Monomer Architecture as a Mechanism to Control the Self-Assembly of Oligomeric Diblock Peptide-Polymer Amphiphiles

Benjamin P. Allen[a], Sabila K. Pinky[b], Emily E. Beard[a], Abigail A. Gringeri[a], Nicholas Calzadilla[a], Matthew A. Sanders[a], Yaroslava G. Yingling*[b], and Abigail S. Knight*[a]

[a] B.Allen, E. Beard, A. Gringeri, N. Calzadilla, M. Sanders, Prof. A. Knight
Department of Chemistry
University of North Carolina at Chapel Hill
Chapel Hill, North Carolina 27599, United States
E-mail: aknight@unc.edu

[b] S. K. Pinky, Prof. Y. Yingling
Department of Materials Science and Engineering
North Carolina State University
Raleigh, North Carolina 27695, United States
E-mail: yara_yingling@ncsu.edu

Abstract Diblock oligomeric peptide-polymer amphiphiles (PPAs) are biohybrid materials that offer versatile functionality by integrating the sequence-dependent properties of peptides with the synthetic versatility of polymers. Despite their potential as biocompatible materials, the rational design of PPAs for assembly into multi-chain nanoparticles remains challenging due to the complex intra- and intermolecular interactions emanating from the polymer and peptide segments. To systematically explore the impact of monomer architecture on nanoparticle assembly, PPAs were synthesized with a random coil peptide (XTEN2) and oligomeric alkyl acrylates with unique side chains: ethyl, *tert*-butyl, *n*-butyl, and cyclohexyl. Experimental characterization using electron and atomic force microscopies demonstrated that tail hydrophobicity impacted accessible morphologies. Moreover, characterization of different assembly protocols (i.e., bath sonication and thermal annealing) revealed that certain tail architectures provide access to kinetically trapped assemblies. All-atom molecular dynamics simulations of micelle structure formation unveiled key interactions and differences in hydration states, dictating PPA assembly behavior. These findings highlight the complexity of PPA assembly dynamics and serve as valuable benchmarks to guide the design of PPAs for a variety of applications including catalysis, mineralization, targeted sequestration, antimicrobial activity, and cargo transportation.

Introduction

Multi-chain nanoparticles are instrumental in nanotechnology and nanomedicine,[1,2] serving as versatile chemosensors[3] and with applications in organic semiconductors[4,5] and biomineralization[6,7]. Despite their wide-ranging applications, their rational design remains challenging due to the complex network of inter- and intramolecular interactions formed between macromolecules. Many nanoparticles are assembled through the phase separation of hydrophobic and hydrophilic blocks in aqueous solution. While hydrophobic interactions predominantly drive this self-assembly, the assembled morphologies are further influenced by a concert of non-covalent interactions (e.g., electrostatics, van der Waals, π-π stacking, and hydrogen bonding) and processing steps such as the assembly technique and filtration.[2,7–9] This interplay of variables provides tunability of both nanoparticle morphology and size, consequently dictating the functionality of the assembled structure. Therefore, understanding the interplay of these interactions is paramount in the rational design of functional nanoparticles.

Peptide amphiphiles (PAs) uniquely incorporate protein-like functions into assembled nanostructures when coupled to a hydrophobic tail.[1,7,10,12,13] Assembled PAs can template biomineralization of inorganic nanoparticles,[11] induce phosphorylation for therapeutics,[12] and outperform the function of their native protein analogs[13,14]. While altering the hydrophobic block composition using aromatic moieties, amino acids, and/or multi-chain lipid-like tails modulates the assembled morphology, these moieties have a narrow scope of easily accessible hydrophobic tails which limits the range of accessible morphologies and assembly dynamics.

Diblock peptide-polymer amphiphiles (PPAs) are biohybrid materials that combine sequence-defined peptides with oligomeric tails synthesized with common polymerization techniques;[15–17] monomer selection, molecular weight, and dispersity enable tunability of the hydrophobic amphiphile component, which in turn dictates the final assembled morphology.[18–20] We have previously demonstrated that oligomeric diblock PPAs composed of oligo(ethyl acrylate) tails and random-coil peptides exhibit similarities to block copolymers, assembling into nanoparticles with diverse morphological distributions influenced by the average molecular weight and dispersity of the hydrophobic oligomer.[21] Efforts with amphiphilic block copolymers have demonstrated that the chemical composition of pendent moieties can impact both the packing density[8,22] and exchange

dynamics[8,23,24] of multi-chain assemblies. However, the impact of monomer architecture within the hydrophobic tails of PPAs on morphology and assembly dynamics has remained unexplored.

Herein, we investigate the self-assembly of PPAs composed of a random coil peptide and acrylate oligomers with variable monomer chemistry (ethyl, *tert*-butyl, *n*-butyl, and cyclohexyl) using a combination of experimental techniques to probe the morphological distributions and computational methods to provide mechanistic insights. Through experimental characterization by electron and atomic force microscopies, we analyze how both the oligomeric tail hydrophobicity and assembly mechanism impact nanoparticle sizes and morphologies. Additionally, all-atomistic molecular dynamic simulations of the micelle structure of three selected amphiphile assemblies reveal the influence of intramolecular interactions and presence of core hydration, enabling deeper mechanistic insights. This integrated approach highlights the tunability afforded by the hydrophobic component of the PPA, yielding morphological distributions that can be modulated using both hydrophobicity and the assembly mechanism.

Results and Discussion

To investigate how the morphology and dynamics of nanoparticles formed by diblock peptide-polymer amphiphiles (PPA) can be tuned via the hydrophobic oligomeric tail, four alkyl acrylate oligomers were synthesized with consistent degrees of polymerization (DP_{tail}) but variable pendent chain architecture: oligo(ethyl acrylate) (*o*EA), oligo(*tert*-butyl acrylate) (*ot*BA), oligo(*n*-butyl acrylate) (*on*BA), and oligo(cyclohexyl acrylate) (*oc*HA) (Figure 1a). The oligomers were synthesized using atom transfer radical polymerization with a protected maleimide initiator to facilitate both coupling to a cysteine-containing peptide and access to short oligomers with controlled molecular weight dispersity (Figures S1-S2).[25] Post polymerization, the oligomers were substituted with propanethiol, removing the bromine chain end to prevent off-target reactions. The maleimide chain end was then deprotected under vacuum and heated to generate a reactive handle for peptide coupling (Figures 1b and S3-S18).[21] To limit the impact of peptide secondary structure and incorporate a hydrophilic block capable of solubilizing the series of hydrophobic oligomers, we chose the charged random coil peptide XTEN2 containing 17 amino acids (Figures 1c and S19).[26,27] XTEN2 was synthesized using solid phase peptide synthesis, incorporating an N-terminal cysteine residue to couple the peptide with the deprotected maleimide terminus of each of the hydrophobic oligomers. Following purification of the peptide using reversed-phase high performance liquid chromatography (HPLC), the thiol-maleimide coupling was facilitated by 4-(2-hydroxyethyl)-1-piperazineethanesulfonic acid (HEPES, 20x) and tris(2-carboxylethyl)phosphine (TCEP, 2x) in DMF at 85 °C. Purification of the amphiphiles was accomplished using disposable reversed-phase columns to remove unreacted peptide and polymer from the amphiphile. After purification, characterization via liquid chromatography-mass spectrometry (LC-MS) enabled calculation of the average degree of polymerization (DP_{tail}), number average molecular weight (M_n), and weight average molecular weight (M_w) of each amphiphile (Figures 1d and S20-S24). The PPA series has a consistent average DP_{tail} of 5 and a low dispersity ($Đ \approx 1$), facilitating a minimized impact of these variables on the nanoparticle assemblies. Additionally, simulations of discrete oligomeric tails (DP_{tail} = 5) visualized using Discovery Studio Visualizer revealed comparable contour lengths (Figure 1d), further supporting that differences in nanoparticle properties amongst the PPA assemblies will primarily be driven by the monomer architecture.

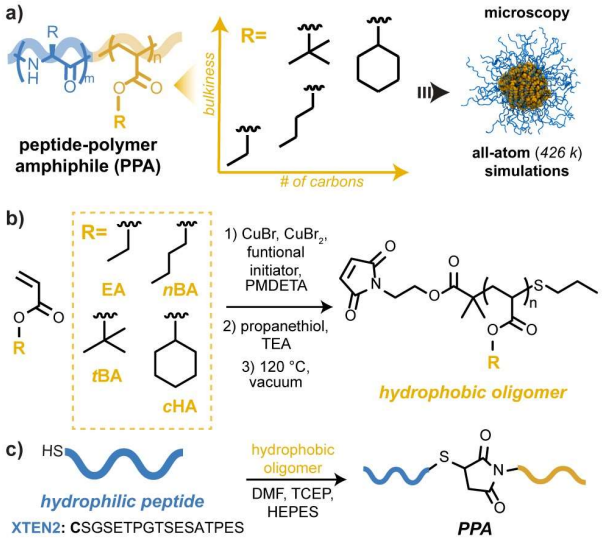

d)

Amphiphile	M_n (g/mol)	M_w (g/mol)	$Đ_{tail}$	DP	Contour Length (Å)
oEA_5-XTEN2	2423	2433	1.00	5.1 ± 1.5	26.1
otBA_5-XTEN2	2525	2544	1.01	4.8 ± 1.7	26.1
onBA_5-XTEN2	2528	2543	1.01	4.8 ± 1.5	26.1
ocHA_5-XTEN2	2647	2666	1.01	4.8 ± 1.4	26.1

Figure 1. Overview of oligomeric diblock peptide-polymer amphiphile (PPA) design and synthesis. (a) Schematic illustrating PPA design containing a series of hydrophobic tails varying the monomer bulkiness and/or carbon number of the pendent moiety and complementary experimental and computational characterization. (b) Alkyl acrylate oligomers were synthesized with a functional initiator containing a protected maleimide and atom transfer radical polymerization with ethyl acrylate (EA), *n*-butyl acrylate (*n*BA), *tert*-butyl acrylate (*t*BA), or cyclohexyl acrylate (*c*HA). Polymerizations were performed in acetone at 50 °C (monomer 25 eq, acetone 50% v/v, functional initiator 1 eq, CuBr 0.5 eq, $Cu(II)Br_2$ 0.025 eq, *N,N,N′,N″,N″*-pentamethyldiethylenetriamine (PMDETA) 0.53 eq) and quenched prior to full conversion. Subsequent thiol substitution of the bromine chain (10 eq propanethiol, 11 eq triethylamine (TEA), rt, on) and deprotection (120 °C, 2h) formed oligomers with terminal maleimides. (c) The XTEN2 peptide was coupled to the maleimide using an N-terminal cysteine residue using 4-(2-hydroxyethyl)-1-piperazineethanesulfonic acid (HEPES, 20x) and tris(2-carboxylethyl)phosphine (TCEP, 2x) in DMF (85 °C, 5h). (d) The number average molecular weight (M_n), weight average molecular weight (M_w), molecular weight dispersity (Đ), and average degree of polymerization (DP_{tail}) for each PPA oligomer tail calculated by integrating chromatograms obtained from HPLC. Contour length (Å) was calculated for each PPA using Discovery Studio Visualizer.

To evaluate the impact of tail architecture on the accessible assembled morphologies, each amphiphile (1 mM) was assembled in HEPES buffer (50 mM, pH 7) via bath sonication (1 h).[21] The assemblies were visualized via negatively-stained transmission electron microscopy (NS-TEM) (Figures 2a and S25-S28), showing a mixture of spherical particles and supramolecular assemblies of cylinders. Cryogenic electron microscopy (cryo-EM) of the four PPA assemblies confirmed spherical particles to be mixtures of micelles and larger nanostructures with an empty cavity, which we describe as vesicle-like (Figure 2b).[28–30] Cylindrical bundles were challenging to observe via cryo-EM; thus, we further characterized the assembled morphologies using in-solution atomic force microscopy (AFM; Figures 2c and S29-S32) to confirm the bundles are present in solution. AFM confirmed the presence of spherical particles in all PPA assemblies and supramolecular assemblies of cylinders in *on*BA_5-XTEN2 and *oc*HA_5-XTEN2 (Figure S32). While the cylindrical bundles for onBA5-XTEN2 and ocHA5-XTEN2 exhibit well-defined bundles (average diameter = 23 ± 2 nm; Figure S31), ocHA5-XTEN2 forms larger heterogenous assemblies (Figure S32). We also note that these bundles are present even one week following the initial assembly (Figure S33). Similar supramolecular assemblies have been observed with gemini amphiphiles that have interparticle associations stabilized by interactions between the hydrophilic interfaces.[31,32] We hypothesize that, analogously, electrostatic interactions between the peptides in the cylinder corona stabilize the supramolecular architecture. Supporting this hypothesis, only spherical particles are observed when *on*BA_5-XTEN2 was assembled with an additional 100 mM NaCl that provides charge screening (Figure S33).

After identifying three morphologies formed by PPA assemblies, we sought to quantify differences between the populations formed by each PPA. To measure the diameters of the particles, we developed a semi-automated image quantification protocol. Briefly, NS-TEM images were pre-processed using ImageJ to generate image masks, followed by extraction of the particle diameters using a MATLAB script(Script_Polymer_Analysis)[33] (Scheme S1). To determine the average diameters of the micelle and vesicle-like particles for each PPA assembly, the full spherical particle population was fit to the sum of a Gaussian fit for the micelle population and lognormal fit for the vesicle-like population (Figure 2d).[21,34–37] The peak centers of both fits were used to calculate the average micelle and vesicle-like particle diameters respectively.

Average nanoparticle diameters were similar across the amphiphile assemblies, as anticipated due to the uniform PPA length (Figure 1d); however, differences were observed in the micelle and vesicle-like diameters within the series. Both *o*EA_5-XTEN2 and *on*BA_5-XTEN2 have smaller micelle diameters (10 nm and 9 nm, respectively) than *ot*BA_5-XTEN2 and *oc*HA_5-XTEN2 (12 nm; Figure 2d). The *on*BA_5 and *ot*BA_5 tails are isomers, both containing four carbons in the pendent chain, indicating that differences in particle size are influenced by the architecture. Bulkier side chains have been observed to exhibit restricted interdigitation, diminishing their capacity to interact with adjacent chains during assembly and resulting in the formation of larger nanoparticles.[38] Extending this hypothesis to *ot*BA_5-XTEN2 and *oc*HA_5-XTEN2, the bulky side-chains hinder efficient packing. Leveraging variations in the bulkiness of pendent sidechains provides a strategic approach to fine-tuning nanoparticle size without necessitating modifications to the peptide composition of the PPA.

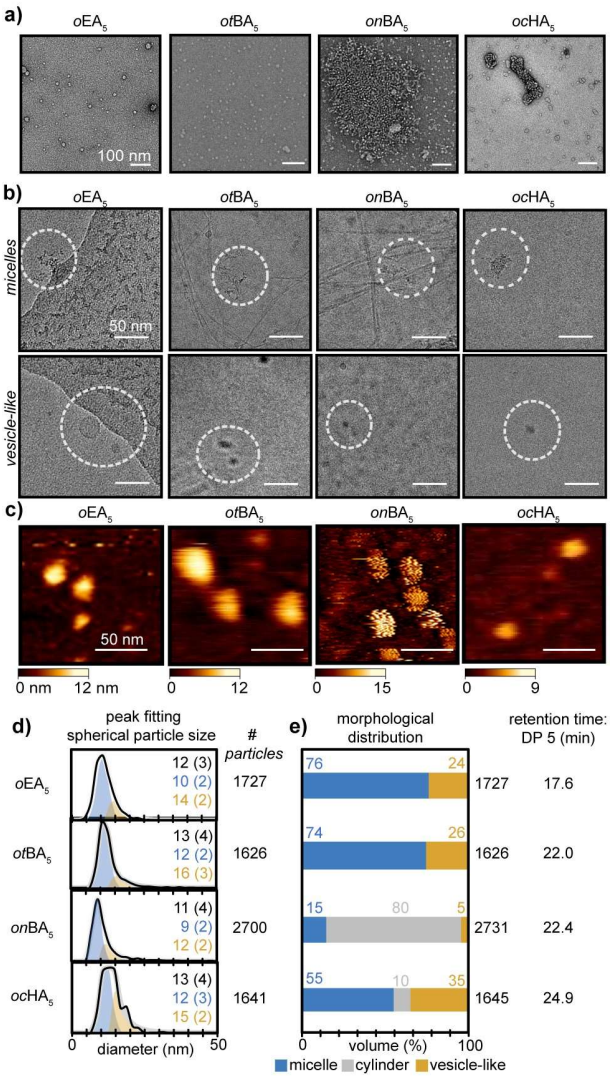

Figure 2: Characterization of PPAs assembled using bath sonication. (a) Representative TEM images for PPAs (left to right): oligo(ethyl acrylate) (*o*EA_5), oligo(*n*-butyl acrylate) (*on*BA_5), oligo(*tert*-butyl acrylate) (*ot*BA_5), and oligo(cyclohexyl acrylate) (*oc*HA_5); scale bars represent 100 nm. (b) Representative cryo-EM images capturing micelles (top row) and vesicle-like particles (bottom row). A white dashed circle is used to indicate the particle(s) of interest. (c) Representative in-solution AFM images for PPAs; scale bars represent 50 nm. Bars located underneath each AFM image reflect the relative height of the particles from the mica surface. (d) Peak fitting applied to the histograms of spherical particle diameters to estimate the population and size for micelles and vesicle-like particles. Black = raw data, blue = Gaussian-fit micelle distribution, yellow = lognormal-fit vesicle-like distribution, and gray = sum of both fits. Average (standard deviation) for total spherical particles (black), micelles (blue) and vesicle-like particles (yellow) diameters are in the top right corner of each histogram. (e) Morphological distributions for each amphiphile based on fitting of histograms and pixel areas for each morphology; blue = micelle, yellow = vesicle-like particles, and gray = cylinders. The LC retention time of the DP_{tail}=5 amphiphile chain for each PPA is listed on the right.

To quantify the ratio of micelles, vesicle-like particles, and cylinders in each PPA assembly, the pixel area of each morphology was calculated from the NS-TEM images and compared to amphiphile hydrophobicity as approximated using the HPLC retention time of comparable oligomers (DP_{tail}=5; Scheme S1, Figure 2e). Analogous to block copolymers,[21,39] more hydrophobic amphiphiles (e.g., *oc*HA_5-XTEN2) form a larger population of vesicle-like particles, an intermediate hydrophobicity leads to cylindrical particle formation (e.g., *on*BA_5-XTEN2), and predominantly micelles are formed by the least hydrophobic amphiphiles, *o*EA_5-XTEN2 and *ot*BA_5-XTEN2 (Figure 2e). Despite the difference in hydrophobicity between *ot*BA_5 and *o*EA_5, their respective PPAs form similar morphological distributions. We hypothesize that the formation of assemblies with lower curvature (i.e., cylindrical assemblies and vesicle-like particles) is stifled for *ot*BA_5-XTEN2 due to limited interdigitation.[40,41] Consequently, the hydrophobicity of the amphiphile and pendent group architecture can be orthogonal tools to tune the morphologies of PPA nanoparticles.

Motivated by the block-copolymer-like behavior exhibited by the PPAs, we sought to determine whether kinetically "frozen" morphologies, typical of amphiphilic block copolymers,[8,24] could be accessed with PPAs. This phenomenon occurs when unimer exchange (i.e., exchange of a single amphiphile between assemblies) is limited due to high interfacial tension between the amphiphile and the solvent. To probe this phenomenon, we selected an additional protocol for amphiphile assembly, thermal annealing, and monitored changes in the assembled morphologies.[24,42,43] Thermal annealing (80 °C, 300 rpm, 1 h followed by cooling to rt) of each PPA in buffer conditions consistent with the sonication-driven assembly similarly yielded multiple particle types observed by NS-TEM and cryo-EM (Figures 3a and S34-S40). In contrast to the sonication-driven assembly, these PPA assemblies had more uniform micelle (8-10 nm) and vesicle-like particle diameters (12-14 nm; Figure 3b). While *o*EA_5-XTEN2 and *on*BA_5-XTEN2 maintain consistent particle diameters between assembly methods, *ot*BA_5-XTEN2 and *oc*HA_5-XTEN2 have reduced micelle and vesicle-like diameters compared to sonication-induced assembly. The decrease in particle sizes suggests tighter packing of the amphiphile chains. This could be attributed to an increase in available energy, allowing chains to overcome their high interfacial tension and rearrange.

In addition to decreasing spherical particle sizes, there is also a change in the morphological distributions; the population of cylindrical bundles decreases for both *on*BA_5-XETN2 and *oc*HA_5-XTEN2 (Figure 3c). Of note, *oc*HA_5-XTEN2 forms primarily vesicle-like nanoparticles when assembled with thermal annealing; similarly, the population of *on*BA_5-XETN2 shifts towards vesicle-like nanoparticles. However, *o*EA_5-XTEN2 and *ot*BA_5-XTEN2 have comparable distributions with both assembly methods. As both experimental and computational studies have suggested that vesicle formation can proceed through cylindrical micelle intermediates,[44–47] we hypothesize that thermal annealing uniquely allows the transition from a cylindrical to a vesicle-like morphology for these PPAs through an increased rate of amphiphile exchange.

The changes in nanoparticle size and/or morphology observed for *ot*BA_5-XTEN2, *on*BA_5-XTEN2, and *oc*HA_5-XTEN2 indicate that these PPAs can access kinetically trapped assemblies.[8] In contrast, we observed no change in the morphological distribution or nanoparticle sizes of *o*EA_5-XTEN2 between the assembly protocols (Figure 3b-c). While this does not confirm that it reaches a thermodynamic equilibrium, it does suggest that *o*EA_5-XTEN2 has a lower interfacial tension and thus higher rate of unimer exchange than the other PPAs.[16] To further probe this observation, we monitored the particle sizes of *o*EA_5-XTEN2 and *ot*BA_5-XTEN2 following incubation at room temperature for one week after the initial assembly, as no shift in morphology was observed for either amphiphile using different assembly mechanisms (Figure 3c). After one week, *o*EA_5-XTEN2 maintained uniform particle sizes as observed by NS-TEM (Figure S41), indicative of rapid unimer equilibrium and a long-lived morphology.[16] In contrast, *ot*BA_5-XTEN2 nanoparticles displayed aggregation after one week (Figure S42), which is common for materials with limited exchange as the particles collide over time.[8]

To investigate the complexities of atomic-level processes driving the PPA assembly dynamics and final structure of micelles, all-atomistic molecular dynamics (AMD) was used. These simulations contained up to 100 PPAs with over 900,000 atoms in explicit solvent, conducted for 500 ns simulation time. Due to the computational expense of such

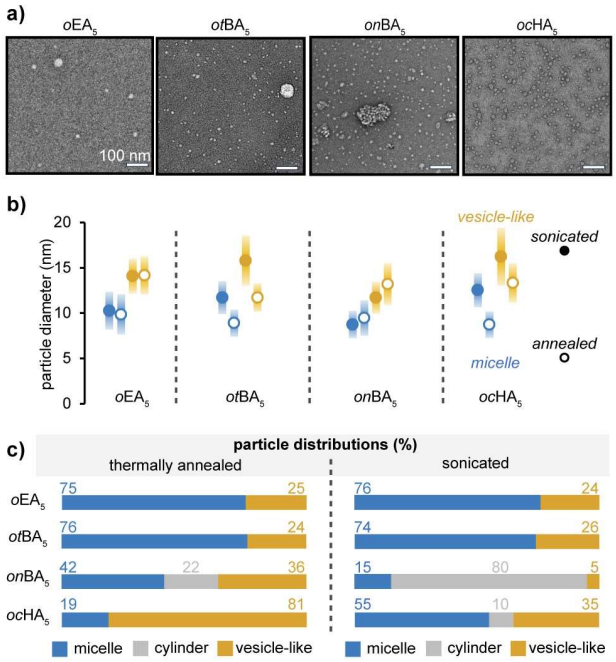

Figure 3: Analysis of negatively stained TEM images of the PPAs assembled by thermal annealing (80 °C, 300 rpm, 1 h, cool rt on). (a) Representative TEM images for each of the four amphiphiles composed of the XTEN2 peptide and each hydrophobic tail; scale bars represent 100 nm. (b) Plot comparing the micelle and vesicle-like particle diameters (standard deviation) for each amphiphile between thermal annealing and sonication-based assembling using fitted histograms. (c) Plot comparing the morphological distributions for each amphiphile for thermal annealing and sonication-based assembly. Blue = micelle, gray = cylinder, and yellow = vesicle-like particles throughout.

simulations, only the isomeric amphiphiles, *on*BA_5-XTEN2 and *ot*BA_5-XTEN2, were selected. Additionally, a lipid control was also screened, C16-XTEN2, as lipid tails are well-studied experimentally and computationally.[48–50] The simulations were initiated from a loosely prearranged spherical micelle shape to decrease the required simulation time (Figure S43). The choice of a total number of simulated amphiphile chains was guided by the aggregation number estimated from experimental characterization of the micelle size and simulated amphiphile volume but was capped at 100 chains due to computational cost (Table S1).

For comparison of acrylate oligomers to a lipid control, the C16-XTEN2 amphiphile was experimentally synthesized by coupling palmitic acid to the N-terminus of an XTEN2 sequence lacking the N-terminal cysteine residue and purification proceeded with semi-preparative HPLC (Figure S44). Self-assembly via thermal annealing of C16-XTEN2 showed micelle formation by both NS-TEM and cryo-EM (Figures S45-S47). To ensure that the number of simulated chains minimally impacted the formation of a micelle and the resultant structure, the C16-XTEN2 amphiphile, containing the fewest atoms, was simulated using 70 chains, corresponding to approximately the experimental aggregation number, and a computationally less expensive 40 chains. The snapshots obtained from the simulations illustrate the final structure of the micelles (Figure 4a), and the simulated micelle diameters ($^sD_{mic}$) were similar to the experimentally derived values ($^eD_{mic}$; Figure 4b). The $^sD_{mic}$ was calculated using the simulation obtained average radius of gyration of the micelle ($^sR_{g(micelle)}$) with the following equation:[51]

$$^sD_{mic} = 2\sqrt{\frac{5}{3}}\,{}^sR_{g(micelle)}$$

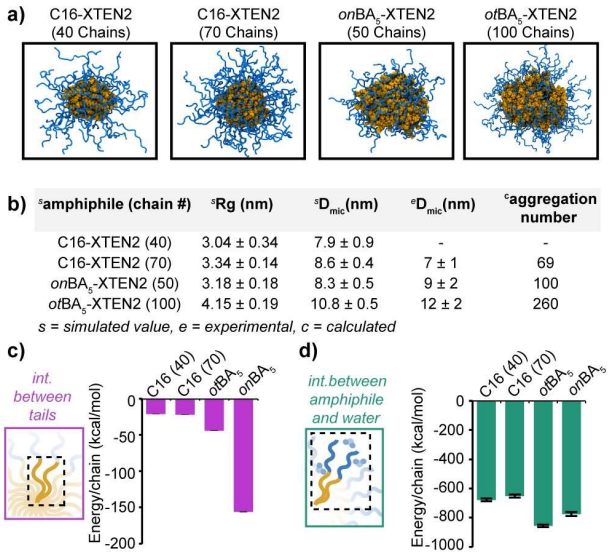

Figure 4. All-atom molecular dynamics simulations of selected amphiphiles. (a) Final snapshots of assembled micelles for C16-XTEN2 (40 chains and 70 chains), *on*BA_5-XTEN2 (50 chains), and *ot*BA_5-XTEN2 (100 chains) at 500 ns. Water and salt atoms are removed for better visualization. (b) Comparison of simulation obtained parameters (radius of gyration, $^sR_{g(micelle)}$ and micelle diameter, $^sD_{mic}$) and experimentally obtained nanoparticle diameters ($^eD_{mic}$) for each amphiphile, followed by the amphiphiles' calculated aggregation number. (c) Non-bonded interaction energy calculated between tails averaged per chain. (d) Non-bonded interaction energy calculated between amphiphiles and water averaged per chain.

Notably, comparable values were obtained for the two C16-XTEN2 simulations, suggesting tolerance in the number of chains used in the simulation.

To understand key interactions dictating micellar structure, non-bonded interaction energies between amphiphilic chains or the surrounding environment were computed from the simulations *(*Figure S49). Interactions between the hydrophobic tails within the micelle core correlate with the experimentally observed hydrophobicity calculated using the amphiphile retention time: the weakest interactions per chain were observed for C16, followed by *ot*BA_5, then *on*BA_5 (Figures 4c and 2e, C16-XTEN2 retention time = 19.7 min). Additionally, the two simulations of C16-XTEN2 (40 and 70 chains) provided consistent energetic values per chain, suggesting that the chemical structure of the tail is more important than the number of chains used in the simulation. Finally, the strength of the tail-tail interactions further supports our hypothesis that *on*BA_5 containing amphiphiles can more easily access lower curvature morphologies with more self-interactions than *ot*BA_5.

To probe the relationship between tail architecture and interfacial tension, we calculated the non-bonded interaction energy between water and the selected amphiphiles (Figure 4d). Notably, the C16 amphiphile (40 and 70 chains) exhibits the lowest non-bonded interaction energy with water, while *ot*BA_5-XTEN2 has a higher energy per-chain as compared to *on*BA_5-XTEN2. This indicates a higher interfacial tension for the PPAs as compared to C16-XTEN2, which aligns with the observation of kinetically "frozen" assemblies for *ot*BA_5-

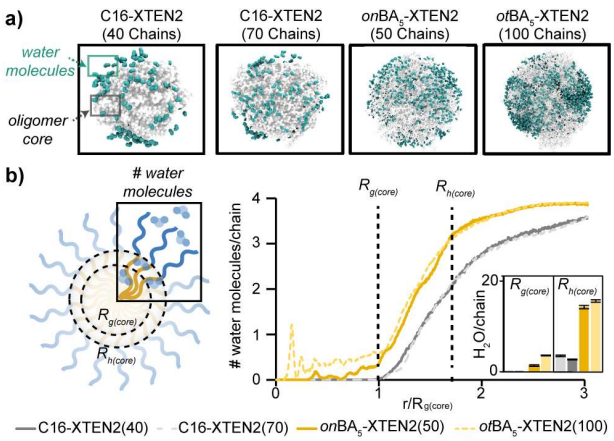

Figure 5: Characterization of water inside the hydrophobic core of peptide amphiphiles. (a) Snapshots of water molecules (teal) within the first water shell (3.4 Å) of the amphiphile core (white) (left to right: C16-XTEN2 (40 chains and 70 chains), *on*BA_5-XTEN2 (50 chains), and otBA5-XTEN2 (100 chains)). (b) (Left) Schematic of the radius of gyration of core ($R_{g(core)}$) and radius of hydration of core ($R_{h(core)}$). (Right) Plot of the radial distribution function of water, distance (r) normalized by the radius of gyration of core, for C16-XTEN2 (40 chains; solid dark gray), C16-XTEN2 (70 chains; light dashed gray), *on*BA_5-XTEN2 (50 chains; solid dark yellow), and *ot*BA_5-XTEN2 (100 chains; dashed light yellow). Black dashed vertical lines illustrate $R_{g(core)}$ and $R_{h(core)}$. Inset plot shows a bar plot of the number of waters per amphiphile chain of amphiphiles in both the $R_{g(core)}$ and $R_{h(core)}$.

XTEN2 and *on*BA_5-XTEN2. Further, an increased volume of the hydrophobic block has been shown to increase amphiphile interfacial tension,[23,52] which is consistent with *ot*BA_5-XTEN2 having a higher energy than *on*BA_5-XTEN2 (Table S2).

As water molecules play a significant role in micelle formation, we analyzed the water molecules present within the assembled structures. Both C16-XTEN2 micelles have a dehydrated core with water present only in the outer shell (Figure 5). Conversely, both *on*BA5-XTEN2and *ot*BA_5-XTEN2 have water inside their cores (the radius of gyration and hydration of the micelle core, $R_{g(core)}$ and $R_{h(core)}$, respectively). Although the hydration of hydrophobic tails is energetically unfavorable, we hypothesize that the presence of hydrophilic ester groups in the oligomeric tail backbone enables the penetration of water molecules inside the hydrophobic core
.[53]

Since the total number of hydrophilic groups within the *ot*BA_5 *on*BA5 tails is the same, we expected a similar number of water molecules inside each core. However, we observed a higher water density inside the core of *ot*BA_5-XTEN2 as compared to *on*BA5-XTEN2 (Figure 5b). Notably, the water molecules inside the core of both *on*BA5-XTEN2 and *ot*BA_5-XTEN2 are dynamic, as visualized over the last 15 ns of the simulations (Figure S50 and Video S1). We have previously observed that a small structural change in the conformation of biopolymers can lead to different amounts of water trapped inside coacervates.[54] Hence, despite having the same number of carbon atoms in the side chain, we hypothesize the bulkiness of the *ot*BA side chain prohibits high density packing of amphiphile chains, enabling greater accommodation of water molecules during the self-assembly process. The presence of water-rich domain inside the oligomer cores supports their ability to form vesicle-like materials,[28–30] contributing to the complex landscape of morphologies formed by the PPAs.

Conclusion

Through this systematic study of diblock oligomeric peptide-polymer amphiphile (PPA) assemblies, we have elucidated the impact of monomer architecture on nanoparticle morphology and dynamics. This work demonstrates that increasing oligomer block hydrophobicity, while maintaining block length, results in predictable morphological trends. Additionally, higher hydrophobic volumes lead to kinetically trapped nanoparticles due to an elevated interfacial tension with water. This affords orthogonal tunability of nanoparticle size and morphology through different self-assembly methods, including bath sonication and thermal annealing. Furthermore, all-atomistic molecular dynamics simulations revealed correlations between non-bonded interaction energies and experimental characterization of hydrophobicity, in addition to offering a valuable tool for characterizing interfacial tension of amphiphiles. Moreover, these simulations revealed variable hydration of the hydrophobic cores, highlighting the significance of subtle structural variations in tail composition. Overall, these findings highlight the intricate tunability PPAs offer for controlled nanoparticle formation, providing a modular platform for the rational design of bioinspired functional assemblies.

Future research with PPAs is poised to continue to integrate the synthetic versatility of polymers with the biomimetic capabilities of peptides to better emulate and expand on natural functionality. Fine-tuning the molecular weight dispersity could enable access to specific morphologies mimicking natural organelles or biophysical properties such as controlled membrane fluidity, which is critical for drug delivery. Further, the use of functional peptides with requisite secondary structure can allow biomimetic functionality such as metal sequestration and catalysis. PPAs can be further incorporated into biotechnologies and biomedicines by utilizing antimicrobial peptides for targeted cell lysis or assembling into stable nanostructures for energy storage. Understanding how peptide and polymer composition influence hierarchical assemblies will allow biohybrid materials to better emulate biological functionality seen in protein complexes, bringing synthetic materials closer to natural efficacy.

Acknowledgements

This material is based upon experimental work (A.S.K.) supported by the Air Force Office of Scientific Research under Award Number FA9550-20-1-0172 and computational work (Y.G.Y.) supported through the National Science Foundation Macromolecular, Supramolecular, and Nanochemistry Program under Award Number CHE-2108818. B.P.A. thanks the UNC Program in Molecular and Cellular Biophysics (MCBP) National Institutes of Health (NIH) training fellowship (T32GM008570). AFM characterization was supported by the National Institute of General Medical Sciences (NIGMS) (R35 GM127151). TEM was performed in part at the Chapel Hill Analytical and Nanofabrication Laboratory, CHANL, a member of the North Carolina Research Triangle Nanotechnology Network, RTNN, which is supported by the National Science Foundation, Grant ECCS-1542015, as part of the National Nanotechnology Coordinated Infrastructure, NNCI. We acknowledge Dr. Joshua Strauss of the UNC CryoTEM Core Facility and Dr. Kedar Sharma for technical assistance in this project, as well as Will Simke for guidance in the development of the image analysis tool.

References

(1) Dasgupta, A.; Das, D. Designer Peptide Amphiphiles: Self-Assembly to Applications. Langmuir 2019, 35 (33), 10704–10724. https://doi.org/10.1021/acs.langmuir.9b01837.

(2) Cui, H.; Webber, M. J.; Stupp, S. I. Self-Assembly of Peptide Amphiphiles: From Molecules to Nanostructures to Biomaterials. Biopolymers 2010, 94 (1), 1–18. https://doi.org/10.1002/bip.21328.

(3) Pramanik, B.; Ahmed, S.; Singha, N.; Das, D. Self-Assembly Assisted Tandem Sensing of Pd2+ and CN− by a Perylenediimide-Peptide Conjugate. ChemistrySelect 2017, 2 (31), 10061–10066. https://doi.org/10.1002/slct.201701849.

(4) Ahmed, S.; Pramanik, B.; Sankar, K. A.; Srivastava, A.; Singha, N.; Dowari, P.; Srivastava, A.; Mohanta, K.; Debnath, A.; Das, D. Solvent Assisted Tuning of Morphology of a Peptide-Perylenediimide Conjugate: Helical Fibers to Nano-Rings and Their Differential Semiconductivity. Sci. Rep. 2017, 7 (1), 9485. https://doi.org/ 10.1038/s41598-017-09730-z.

(5) Ahmed, S.; Amba Sankar, K. N.; Pramanik, B.; Mohanta, K.; Das, D. Solvent Directed Morphogenesis and Electrical Properties of a Peptide–Perylenediimide Conjugate. Langmuir 2018, 34 (28), 8355–8364. https://doi.org/10.1021/acs.langmuir.8b01750.

(6) Hartgerink, J. D.; Beniash, E.; Stupp, S. I. Self-Assembly and Mineralization of Peptide-Amphiphile Nanofibers. Science 2001, 294, 1684–1689. https://doi.org/10.1126/science.1063187.

(7) Dasgupta, A. Exploring Architectures at the Nanoscale: The Interplay between Hydrophobic Twin Lipid Chains and Head Groups of Designer Peptide Amphiphiles in the Self-Assembly Process and Application. Soft Matter 2016, 12 (19), 4352–4360. https://doi.org/10.1039/c6sm00147e.

(8) Nicolai, T.; Colombani, O.; Chassenieux, C. Dynamic Polymeric Micelles versus Frozen Nanoparticles Formed by Block Copolymers. Soft Matter 2010, 6 (14), 3111–3118. https://doi.org/10.1039/b925666k.

(9) Barbee, M. H.; Wright, Z. M.; Allen, B. P.; Taylor, H. F.; Patteson, E. F.; Knight, A. S. Protein-Mimetic Self-Assembly with Synthetic Macromolecules. Macromolecules 2021, 54 (8), 3585–3612. https://doi.org/10.1021/acs.macromol.0c02826.

(10) Trent, A.; Marullo, R.; Lin, B.; Black, M.; Tirrell, M. Structural Properties of Soluble Peptide Amphiphile Micelles. Soft Matter 2011, 7 (20), 9572–9582. https://doi.org/10.1039/C1SM05862B.

(11) Li, Q.; Wang, Y.; Zhang, G.; Su, R.; Qi, W. Biomimetic Mineralization Based on Self-Assembling Peptides. Chem. Soc. Rev. 2023, 52 (5), 1549–1590. https://doi.org/10.1039/D2CS00725H.

(12) Hendricks, M. P.; Sato, K.; Palmer, L. C.; Stupp, S. I. Supramolecular Assembly of Peptide Amphiphiles. Acc. Chem. Res. 2017, 50 (10), 2440–2448. https://doi.org/10.1021/acs.accounts.7b00297.

(13) Mardilovich, A.; Craig, J. A.; McCammon, M. Q.; Garg, A.; Kokkoli, E. Design of a Novel Fibronectin-Mimetic Peptide−Amphiphile for Functionalized Biomaterials. Langmuir 2006, 22 (7), 3259–3264. https://doi.org/10.1021/la052756n.

(14) Kokkoli, E.; Mardilovich, A.; Wedekind, A.; Rexeisen, E. L.; Garg, A.; Craig, J. A. Self-Assembly and Applications of Biomimetic and Bioactive Peptide-Amphiphiles. Soft Matter 2006, 2 (12), 1015–1024. https://doi.org/10.1039/b608929a.

(15) Shu, J. Y.; Panganiban, B.; Xu, T. Peptide-Polymer Conjugates: From Fundamental Science to Application. Annu. Rev. Phys. Chem. 2013, 64 (1), 631–657. https://doi.org/10.1146/annurev-physchem-040412-110108.

(16) Wright, D. B.; Ramírez-Hernández, A.; Touve, M. A.; Carlini, A. S.; Thompson, M. P.; Patterson, J. P.; De Pablo, J. J.; Gianneschi, N. C. Enzyme-Induced Kinetic Control of Peptide-Polymer Micelle Morphology. ACS Macro Lett. 2019, 8 (6), 676–681. https://doi.org/10.1021/acsmacrolett.8b00887.

(17) Callmann, C. E.; Thompson, M. P.; Gianneschi, N. C. Poly (Peptide): Synthesis, Structure, and Function of Peptide–Polymer Amphiphiles and Protein-like Polymers. Acc. Chem. Res. 2020, 53 (2), 400–413. https://doi.org/10.1021/acs.accounts.9b00518.

(18) Doncom, K. E. B.; Blackman, L. D.; Wright, D. B.; Gibson, M. I.; O'Reilly, R. K. Dispersity Effects in Polymer Self-Assemblies: A Matter of Hierarchical Control. Chem. Soc. Rev. 2017, 46 (14), 4119–4134. https://doi.org/10.1039/c6cs00818f.

(19) Jiang, Y.; Chen, T.; Ye, F.; Liang, H.; Shi, A. C. Effect of Polydispersity on the Formation of Vesicles from Amphiphilic Diblock Copolymers. Macromolecules 2005, 38 (15), 6710–6717. https://doi.org/10.1021/ma050424j.

(20) Blanazs, A.; Armes, S. P.; Ryan, A. J. Self-assembled Block Copolymer Aggregates: From Micelles to Vesicles and Their Biological Applications. Macromol. Rapid Commun. 2009, 30 (4-5), 267–277. https://doi-org/10.1002/marc.200800713.

(21) Allen, B. P.; Wright, Z. M.; Taylor, H. F.; Oweida, T. J.; Kader-Pinky, S.; Patteson, E. F.; Bucci, K. M.; Cox, C. A.; Senthilvel, A. S.; Yingling, Y. G.; Knight, A. S. Mapping the Morphological Landscape of Oligomeric Di-block Peptide–Polymer Amphiphiles. Angew. Chem. Int. Ed. 2022. https://doi.org/10.1002/anie.202115547. 61 (14), e202115547.

(22) Kranenburg, M.; Venturoli, M.; Smit, B. Phase Behavior and Induced Interdigitation in Bilayers Studied with Dissipative Particle Dynamics. J. Phys. Chem. B 2003, 107 (41), 11491–11501. https://doi-org.libproxy.lib.unc.edu/10.1021/jp035007s.

(23) Creutz, S.; van Stam, J.; Antoun, S.; De Schryver, F. C.; Jérôme, R. Exchange of Polymer Molecules between Block Copolymer Micelles Studied by Emission Spectroscopy. A Method for the Quantification of Unimer Exchange Rates. Macromolecules 1997, 30 (14), 4078–4083. https://doi-org/10.1021/ma961922i.

(24) Murphy, R. P.; Kelley, E. G.; Rogers, S. A.; Sullivan, M. O.; Epps III, T. H. Unlocking Chain Exchange in Highly Amphiphilic Block Polymer Micellar Systems: Influence of Agitation. ACS Macro Lett. 2014, 3 (11), 1106–1111. https://doi-org/10.1021/mz500435d.

(25) Matyjaszewski, K. Atom Transfer Radical Polymerization (ATRP): Current Status and Future Perspectives. Macromolecules 2012, 45 (10), 4015–4039. https://doi.org/10.1021/ma3001719.

(26) Schellenberger, V.; Wang, C. W.; Geething, N. C.; Spink, B. J.; Campbell, A.; To, W.; Scholle, M. D.; Yin, Y.; Yao, Y.; Bogin, O.; Cleland, J. L.; Silverman, J.; Stemmer, W. P. C. A Recombinant Polypeptide Extends the in Vivo Half-Life of Peptides and Proteins in a Tunable Manner. Nat. Biotechnol. 2009, 27 (12), 1186–1190. https://doi.org/10.1038/nbt.1588.

(27) Podust, V. N.; Balan, S.; Sim, B. C.; Coyle, M. P.; Ernst, U.; Peters, R. T.; Schellenberger, V. Extension of in Vivo Half-Life of Biologically Active Molecules by XTEN Protein Polymers. J. Controlled Release 2016, 240, 52–66. https://doi.org/10.1016/j.jconrel.2015.10.038.

(28) Xiao, M.; Xia, G.-J.; Wang, R.; Xie, D. Controlling the Self-Assembly Pathways of Amphiphilic Block Copolymers into Vesicles. Soft Matter 2012, 8, (30), 7865–7874. https://doi.org/10.1039/C2SM25281C.(29) He, X.; Schmid, F. Dynamics of Spontaneous Vesicle Formation in Dilute Solutions of Amphiphilic Diblock Copolymers. Macromolecules 2006, 39 (7), 2654–2662. https://doi.org/10.1021/ma052536g.

(30) Baoukina, S.; Monticelli, L.; Risselada, H. J.; Marrink, S. J.; Tieleman, D. P. The Molecular Mechanism of Lipid Monolayer Collapse. Proc. Natl. Acad. Sci. 2008, 105 (31), 10803–10808. https://doi.org/10.1073/pnas.0711563105.
(31) Chen, H.; Chen, J.; Wan, D.; Zhang, H.; Mao, C.; Wang, R. Self-assembly of Gemini Amphiphiles with Symmetric Tails in Selective Solvent. Polym. Int. 2022, 71 (9), 1082–1089.
(32) Limouzin-Morel, C.; Dutertre, F.; Moussa, W.; Gaillard, C.; Iliopoulos, I.; Bendejacq, D.; Nicolaï, T.; Chassenieux, C. One and Two Dimensional Self-Assembly of Comb-like Amphiphilic Copolyelectrolytes in Aqueous Solution. Soft Matter 2013, 9 (37), 8931–8937.
(33) Https://Github.Com/UNC-Knight-Lab/Particle-Counting.
(34) Nelson, P. H.; Rutledge, G. C.; Hatton, T. A. On the Size and Shape of Self-Assembled Micelles. J. Chem. Phys. 1997, 107 (24), 10777–10781. https://doi.org/10.1063/1.474193.
(35) Bug, A. L. R.; Cates, M. E.; Safran, S. A.; Witten, T. A. Theory of Size Distribution of Associating Polymer Aggregates. I. Spherical Aggregates. J. Chem. Phys. 1987, 87 (3), 1824–1833. https://doi.org/10.1063/1.453195.
(36) Chécot, F.; Brûlet, A.; Oberdisse, J.; Gnanou, Y.; Mondain-Monval, O.; Lecommandoux, S. Structure of Polypeptide-Based Diblock Copolymers in Solution: Stimuli-Responsive Vesicles and Micelles. Langmuir 2005, 21 (10), 4308–4315. https://doi.org/10.1021/la0468500.
(37) Song, N. W.; Park, K. M.; Lee, I. H.; Huh, H. Uncertainty Estimation of Nanoparticle Size Distribution from a Finite Number of Data Obtained by Microscopic Analysis. Metrologia 2009, 46 (5), 480–488. https://doi.org/10.1088/0026-1394/46/5/012.
(38) Mei, J.; Bao, Z. Side Chain Engineering in Solution-Processable Conjugated Polymers. Chem. Mater. 2014, 26 (1), 604–615. https://doi-org/10.1021/cm4020805.
(39) Foster, J. C.; Akar, I.; Grocott, M. C.; Pearce, A. K.; Mathers, R. T.; O'Reilly, R. K. 100th Anniversary of Macromolecular Science Viewpoint: The Role of Hydrophobicity in Polymer Phenomena. ACS Macro Lett. 2020, 9 (11), 1700–1707.
(40) Razzell-Hollis, J.; Fleischli, F.; Jahnke, A. A.; Stingelin, N.; Seferos, D. S.; Kim, J.-S. Effects of Side-Chain Length and Shape on Polytellurophene Molecular Order and Blend Morphology. J. Phys. Chem. C 2017, 121 (4), 2088–2098. Razzell-Hollis, J.; Fleischli, F.; Jahnke, A. A.; Stingelin, N.; Seferos, D. S.; Kim, J.-S. Effects of Side-Chain Length and Shape on Polytellurophene Molecular Order and Blend Morphology. J. Phys. Chem. C 2017, 121 (4), 2088–2098. https://doi-org/10.1021/acs.jpcc.6b11675.
(41) Balakrishnan, K.; Datar, A.; Naddo, T.; Huang, J.; Oitker, R.; Yen, M.; Zhao, J.; Zang, L. Effect of Side-Chain Substituents on Self-Assembly of Perylene Diimide Molecules: Morphology Control. J. Am. Chem. Soc. 2006, 128 (22), 7390–7398. https://doi-org/10.1021/ja061810z.
(42) Foster, J. C.; Varlas, S.; Couturaud, B.; Jones, J. R.; Keogh, R.; Mathers, R. T.; O'Reilly, R. K. Predicting Monomers for Use in Polymerization-Induced Self-Assembly. Angew. Chem. Int. Ed. 2018, 57 (48), 15733–15737. https://doi-org/10.1002/anie.201809614.
(43) Schroeder, A.; Kost, J.; Barenholz, Y. Ultrasound, Liposomes, and Drug Delivery: Principles for Using Ultrasound to Control the Release of Drugs from Liposomes. Chem. Phys. Lipids 2009, 162 (1–2), 1–16. https://doi-org/10.1016/j.chemphyslip.2009.08.003.
(44) Egelhaaf, S. U.; Schurtenberger, P. Micelle-to-Vesicle Transition: A Time-Resolved Structural Study. Phys. Rev. Lett. 1999, 82 (13), 2804. https://doi.org/10.1103/PhysRevLett.82.2804.
(45) Figg, C. A.; Carmean, R. N.; Bentz, K. C.; Mukherjee, S.; Savin, D. A.; Sumerlin, B. S. Tuning Hydrophobicity to Program Block Copolymer Assemblies from the inside Out. Macromolecules 2017, 50 (3), 935–943. https://doi-org/10.1021/acs.macromol.6b02754.
(46) Chen, L.; Shen, H.; Eisenberg, A. Kinetics and Mechanism of the Rod-to-Vesicle Transition of Block Copolymer Aggregates in Dilute Solution. J. Phys. Chem. B 1999, 103 (44), 9488–9497. https://doi.org/10.1021/jp9913665.
(47) Zhang, L.; Sevink, A.; Schmid, F. Hybrid Lattice Boltzmann/Dynamic Self-Consistent Field Simulations of Microphase Separation and Vesicle Formation in Block Copolymer Systems. Macromolecules 2011, 44 (23), 9434–9447. https://doi.org/10.1021/ma2018638.
(48) Manandhar, A.; Kang, M.; Chakraborty, K.; Tang, P. K.; Loverde, S. M. Molecular Simulations of Peptide Amphiphiles. Org. Biomol. Chem. 2017, 15 (38), 7993–8005. https://doi.org/10.1039/c7ob01290j.
(49) M. Frederix, P. W. J.; Patmanidis, I.; J. Marrink, S. Molecular Simulations of Self-Assembling Bio-Inspired Supramolecular Systems and Their Connection to Experiments. Chem. Soc. Rev. 2018, 47 (10), 3470–3489. https://doi.org/10.1039/C8CS00040A.
(50) McCullagh, M.; Prytkova, T.; Tonzani, S.; Winter, N. D.; Schatz, G. C. Modeling Self-Assembly Processes Driven by Nonbonded Interactions in Soft Materials. J. Phys. Chem. B 2008, 112 (34), 10388–10398. https://doi.org/10.1021/jp803192u.
(51) Bogusz, S.; Venable, R. M.; Pastor, R. W. Molecular Dynamics Simulations of Octyl Glucoside Micelles: Structural Properties. J. Phys. Chem. B 2000, 104 (23), 5462–5470. https://doi.org/10.1021/jp000159y.
(52) Stafford, R. E.; Fanni, T.; Dennis, E. A. Interfacial Properties and Critical Micelle Concentration of Lysophospholipids. Biochemistry 1989, 28 (12), 5113–5120. https://doi-org/10.1021/bi00438a031.
(53) Menger, F.; Jerkunica, J.; Johnston, J. The Water Content of a Micelle Interior. The Fjord vs. Reef Models. J. Am. Chem. Soc. 1978, 100 (15), 4676–4678. https://doi-org/10.1021/ja00483a008.
(54) Li, N. K.; Xie, Y.; Yingling, Y. G. Insights into Structure and Aggregation Behavior of Elastin-like Polypeptide Coacervates: All-Atom Molecular Dynamics Simulations. J. Phys. Chem. B 2021, 125 (30), 8627–8635. https://doi.org/10.1021/acs.jpcb.1c02822.